

STM/STS Study on $4a \times 4a$ Electronic Charge Order and Inhomogeneous Pairing Gap in Superconducting $\text{Bi}_2\text{Sr}_2\text{CaCu}_2\text{O}_{8+\delta}$

A. Hashimoto, N. Momono, M. Oda, and M. Ido

Department of Physics, Hokkaido University, Sapporo 060-0810, Japan

(Dated: March 28, 2020)

We performed STM/STS measurements on underdoped Bi2212 crystals with doping levels $p \sim 0.11$ and ~ 0.14 to study the nature of the nondispersing $4a \times 4a$ charge order in the superconducting state at $T \ll T_c$. The charge order appears conspicuously within the pairing gap, and its period λ slightly depends on the doping level; λ is $4a$ for $p \sim 0.11$ and $\sim 4.2a$ for $p \sim 0.14$. The $\sim 4a \times 4a$ charge order will be dynamical in itself, and pinned down over regions with effective pinning centers. We also point out that the pinned $\sim 4a \times 4a$ charge order is closely related to the spatially inhomogeneous pairing-gap structure, which has often been reported in STS measurements on high- T_c cuprates.

PACS numbers: 74.25.Jb, 74.50.+r, 74.72.Hs

I. INTRODUCTION

Clarification of the nature of the pseudogap state is expected to provide a clue to the mechanism of high- T_c superconductivity. The pseudogap state appears even in lightly doped regions of $\text{Ca}_{2-x}\text{Na}_x\text{CuO}_2\text{Cl}_2$ (Na-CCOC) and $\text{Bi}_2\text{Sr}_2\text{CaCu}_2\text{O}_{8+\delta}$ (Bi2212), where the pseudogap is of an asymmetric, V-shaped type at very low temperatures and has been referred to as the zero temperature pseudogap (ZTPG).^{1,2} It was recently revealed by STM/STS studies that in the ZTPG regime a nondispersing $4a \times 4a$ charge order appears in the two-dimensional (2-d) spatial map of energy-resolved differential tunneling conductance dI/dV , which is proportional to the local density of states (LDOS).^{1,2} A nondispersing $\sim 4a \times 4a$ charge order, electronic in origin, was also reported in the LDOS maps measured in the pseudogap state of Bi2212 at $T > T_c$.³ Such a spatial structure in the LDOS maps was first observed around the vortex cores of Bi2212 exhibiting pseudogap-like V-shaped STS spectra with no peaks at the gap edge.^{4,5} Such charge orders have attracted much attention because the charge order can be a possible electronic hidden order in the pseudogap state.^{1,3}

In measurements of LDOS maps in the superconducting (SC) state of Bi2212, Hoffman *et al.* and McElroy *et al.* found a strongly dispersive 2-d spatial structure, which has been successfully explained in terms of SC quasiparticle scattering interference.^{6,7} Furthermore, Howald *et al.* and Fang *et al.* reported a nondispersing $\sim 4a \times 4a$ charge order with anisotropy in the SC state of Bi2212 in addition to weakly dispersive ones, and claimed that the charge order was due to the stripe order and coexisted with the superconductivity.^{8,9} However, the nondispersing $\sim 4a \times 4a$ charge order at $T < T_c$ was not confirmed in other LDOS measurements on Bi2212.^{3,6} Very recently the nondispersing $4a \times 4a$ charge order at $T < T_c$ was found to appear in heavily underdoped SC Bi2212.¹⁰ The charge order is commensurate ($4a \times 4a$) and has an internal structure with a period of $4a/3 \times 4a/3$ like the electronic charge order reported by Hanagri *et*

al. for lightly doped Na-CCOC.¹ The observation of the same charge order for both cuprates Na-CCOC and Bi2212 provides definite evidence that the nondispersing $4a \times 4a$ charge order develops on the Cu-O layer. The $4a \times 4a$ charge order is likely to be dynamical in itself, and pinned down over regions with effective pinning centers.¹⁰ To understand the nature of the nondispersing $4a \times 4a$ charge order, it is desirable to investigate the charge order on crystals with different doping levels and/or pinning centers of different natures.

In the present work, we studied the nondispersing $4a \times 4a$ charge order from STM measurements on Bi2212 crystals with different doping levels and/or pinning centers of different properties. We found that low doping favors the development of the $\sim 4a \times 4a$ charge order though it would be dynamical without pinning centers. We also studied the STS spectra over the same region where STM images were taken, and point out that the spatially inhomogeneous gap structure, often reported in STS measurements on high- T_c cuprates,^{11–17} strongly correlates with the appearance of the pinned $\sim 4a \times 4a$ charge order.

II. EXPERIMENTAL PROCEDURES

In the present study, single crystals of Bi2212 were grown using traveling solvent floating zone method. We estimated doping level p of the Cu-O layer from the SC critical temperature T_c determined from the SC diamagnetism and the characteristic temperature T_{\max} of the normal-state magnetic susceptibility; both T_c and T_{\max} follow empirical functions of p .^{18,19} The doping level was controlled by changing the pressure of oxygen atmosphere in the course of growing the crystal. We performed STM/STS measurements at $T \sim 9$ K on two sets of sample pairs; A and B cut from a single crystal with $T_c \sim 72$ K ($p \sim 0.11$), and C and D from a single crystal with $T_c \sim 78$ K ($p \sim 0.14$). In the present STM/STS experiments, Bi2212 crystals were cleaved in an ultrahigh vacuum at ~ 9 K just before the approach of the STM

tip toward the cleaved surface *in situ*. Bi2212 crystals are usually cleaved between the upper and lower layers of the Bi-O bilayer. In Bi2212 crystals, excess oxygen atoms contained within Bi-O bilayers provide Cu-O layers nearby with mobile holes. However, excess oxygen atoms will be appreciably lost during the process of cleaving the crystal at high temperatures. So, to suppress the loss of excess oxygen atoms, i.e. mobile holes, to as low a level as possible, we cleaved the crystals at very low temperatures (~ 9 K). In the present study, STM images of 512×512 pixels were taken over the surface areas of ~ 38 nm \times 38 nm for samples A, C, D and of ~ 23 nm \times 23 nm for sample B in the constant height mode under constant sample bias voltage V_s applied between the tip and the sample. The differential conductance dI/dV was measured by using a standard lock-in technique with an ac bias modulation of 3 mV and a frequency of 4 kHz.

III. RESULTS AND DISCUSSION

A. STM images of Cu-O layer; the $\sim 4a \times 4a$ charge order

The cleaved Bi-O layer of Bi2212 crystals is semiconducting with a gap on the order of 0.1 eV ($\Delta_{\text{Bi}-\text{O}}$). Therefore, if we choose a high bias voltage V_s , which lies outside the semiconducting gap $\Delta_{\text{Bi}-\text{O}}$ where there are electronic states in Bi-O layers, in the STM experiment (Fig. 1(a)), the STM electron-tunneling occurs predominantly between the STM tip and the cleaved Bi-O layer. Thus we can observe the Bi-O layer selectively in STM imaging at a high bias, when we keep the STM tip at a distance from the sample surface. On the other hand, if we choose a low bias V_s , which lies within the semiconducting gap $\Delta_{\text{Bi}-\text{O}}$ where electronic states do not exist in Bi-O layers but in the Cu-O layer (Fig. 1(b)), the STM electron-tunneling can occur between the STM tip and the Cu-O layer which is buried just below the cleaved Bi-O layer. In STM imaging at a low bias, we can observe the Cu-O layer selectively when the STM tip approaches the sample surface so that wave functions of carriers between the STM tip and the Cu-O layer can overlap.²⁰ In fact, STM images taken on sample A at high and low biases had different features, especially, with respect to the missing atom rows inherent in the Bi-O layer, as shown in Figs. 2(a) and (b).²¹ In an STM image taken at 600 mV (high bias), the missing atom rows appear very clearly (Fig. 2(a)). On the other hand, the missing atom rows become very weak in the STM image taken at 30 mV (low bias), as seen in Fig. 2(b). The latter result confirms that in the low-bias STM imaging the STM tunneling mainly occurs between the Cu-O layer with no missing atom rows and the STM tip.

In the low-bias STM image of sample A shown in Fig. 2(b), we can identify a bond-oriented, 2-d superstructure throughout the entire STM image. The 2-d superstructure appeared with the same pattern in both STM

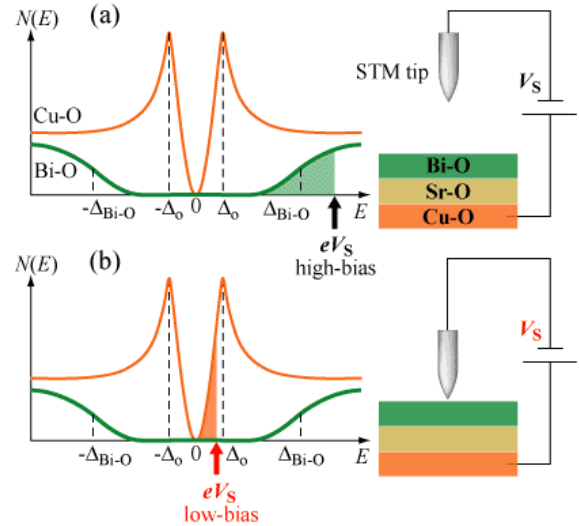


FIG. 1: (Color online) Schematic energy diagram of Bi2212 and illustration of STM measurements at (a) high ($V_s > \Delta_{\text{Bi}-\text{O}}$) and (b) low biases ($V_s < \Delta_{\text{Bi}-\text{O}}$). The density of states $N(E)$ for Cu-O and Bi-O layers are schematically represented by thin and thick lines, respectively. In the high-bias STM experiment, electron tunneling occurs predominantly between the STM tip and the Bi-O layer when the tip-sample separation is large, whereas in the low-bias STM experiment, it occurs between the STM tip and the Cu-O layer when the tip-sample separation is small.

measurements at positive and negative biases. Figure 2(c) shows the line profiles of STM images taken along the solid line shown in Fig. 2(b), for various bias voltages. The 2-d superstructure with a period of $4a$ appears clearly below $V_s \sim 100$ mV in addition to the underlying primitive lattice, and the period of $4a$ is almost independent of bias voltage V_s . The superstructure is more intense at lower biases, while it is very weak above $V_s = 100$ mV. A part of the low-bias STM image, taken on sample B at $V_s = 10$ mV, is shown in Fig. 3(b). The 2-d superstructure appears locally on a nanometer scale, not throughout the entire STM image. In Fig. 3(c), a line profile of the STM image is shown for the area where the clear 2-d superstructure appears locally and compared with that of sample A. This line profile shows that the period of the superstructure is also $4a$ but its amplitude is much smaller than that observed for sample A.

The 2-d superstructure can also be confirmed in the Fourier map $F(q_x, q_y)$ of the low-bias STM images. The Fourier map $F(q_x, q_y)$ of the STM image, taken on sample A at $V_s = 30$ mV, shows that the main Fourier peaks associated with the 2-d superstructure appear at $q = (1/4, 0)$ and $(0, 1/4)$, as shown in Fig. 4(a). This means that the period of the 2-d superstructure is $4a \times 4a$. The Fourier spot at $q = (1/4, 0)$ is stronger than the spot at $q = (0, 1/4)$, indicating that the 2-d superstructure is anisotropic. In Fig. 4(a), a line cut of the Fourier map along the $(\pi, 0)$ direction is also shown for sample A as a

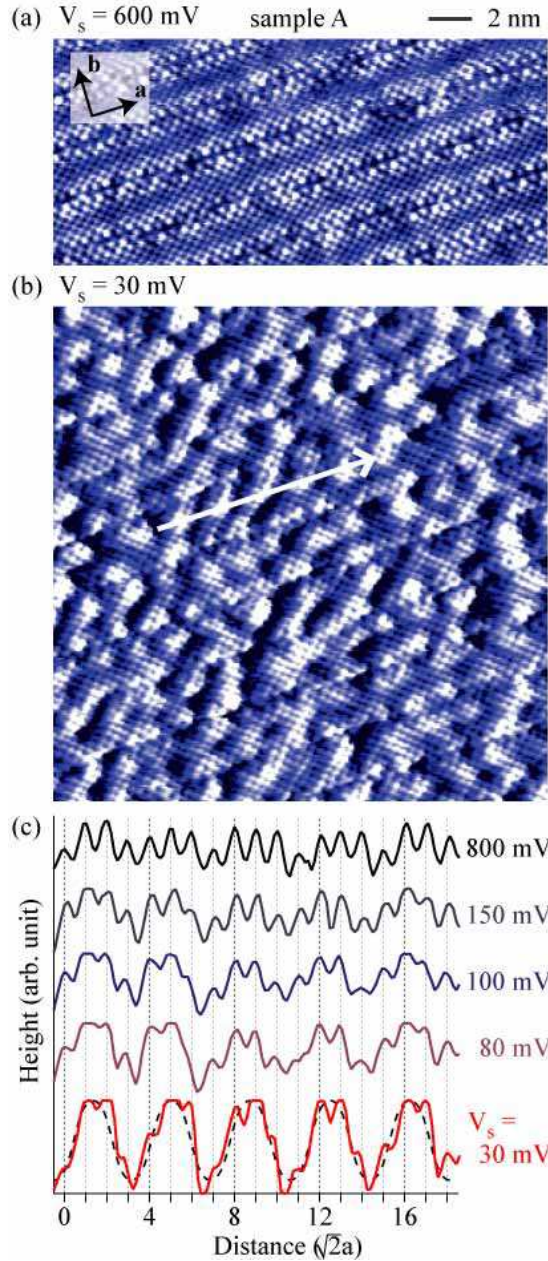


FIG. 2: (Color online) (a) Part of a high-bias STM image of sample A, measured at a bias voltage of $V_s = 600$ mV and an initial tunneling current of $I_t = 0.3$ nA at $T \sim 9$ K. The image shows a one-dimensional (1-d) superlattice, inherent in the Bi-O layer, with missing atom rows. (b) Part of a low-bias STM image of sample A, measured at $V_s = 30$ mV and $I_t = 0.3$ nA at $T \sim 9$ K, showing a $4a \times 4a$ superstructure, together with individual atoms. (c) Line profiles taken along the solid line in the STM image (Fig. (a)) for various bias voltages. The solid line is cut perpendicular to the b axis, that is, 45 degrees from the orientation of the $4a \times 4a$ superstructure so that the 1-d superlattice of the Bi-O layer does not obscure the profile of the $4a \times 4a$ superstructure. Note that, in the line profile for the lowest bias, the spatial variation due to the underlying host lattice is partly cut over the intense $4a \times 4a$ superstructure because of saturation of the STM amplifier.

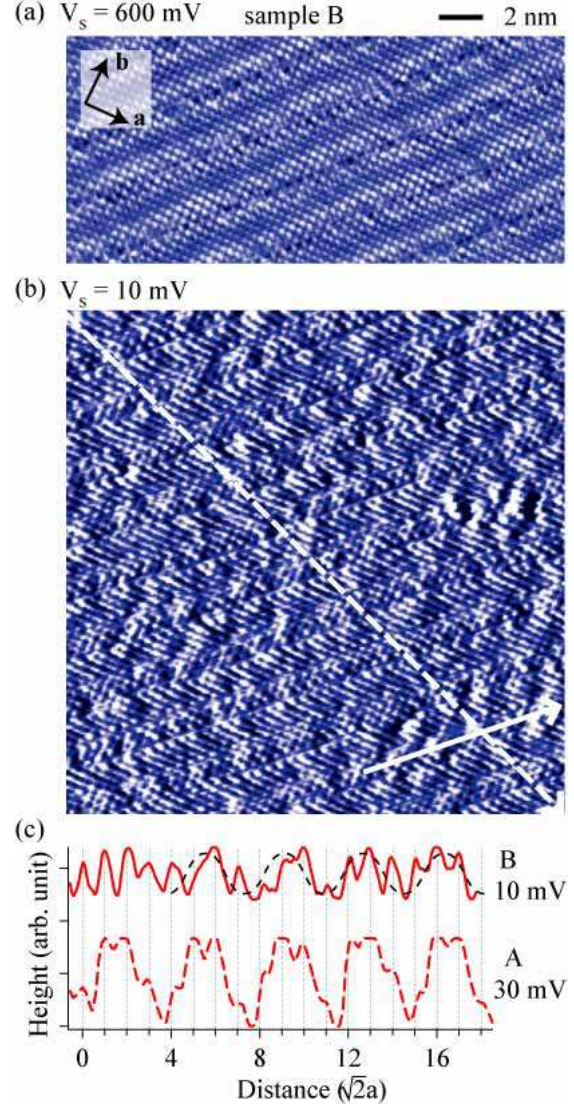


FIG. 3: (Color online) (a) Part of a high-bias STM image of sample B, measured at $V_s = 600$ mV and $I_t = 0.3$ nA at $T \sim 9$ K. Note that it shows almost no missing atom rows in contrast with that of sample A (Fig. 2(a)). (b) Part of a low-bias STM image of sample B, measured at $V_s = 10$ mV and $I_t = 0.3$ nA at $T \sim 9$ K. (c) Line profile of STM image taken along the solid line in Fig. (b) at $V_s = 10$ mV (solid line). For comparison, the line profile at $V_s = 30$ mV for sample A (Fig. 2(c)) is also shown (dashed line). The dashed line for sample B is a guide to the eye.

function of the bias voltage V_s . Each line profile is normalized with the intensity of the Bragg peak at $q = (1, 0)$. Weak Fourier peaks also appear at $q = (3/4, 0)$ in addition to the strong main peak at $q = (1/4, 0)$. Both $q = (1/4, 0)$, $(3/4, 0)$ peaks are most intense at the lowest bias (20 mV), but they decrease rapidly with V_s and become very weak above $V_s \sim 100$ mV. It should be noted here that these Fourier peaks show no change in position and no broadening as V_s increases, providing evidence

that the present $4a \times 4a$ superstructure is nondispersive. The $4a \times 4a$ superstructure can be observed even at 82 K above T_c ($= 72$ K) in sample A, as shown in the inset of Fig. 4(a).

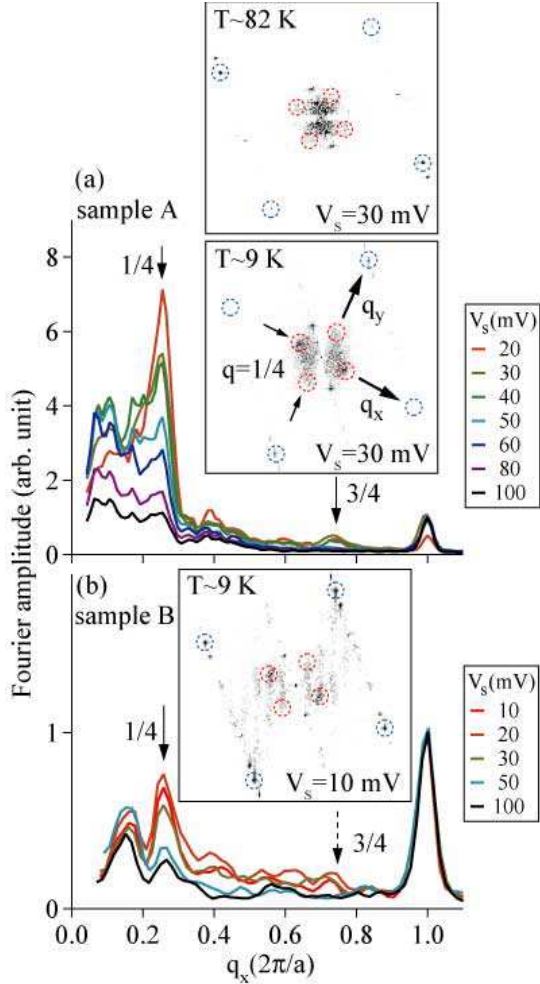


FIG. 4: (Color) (a) Fourier maps of the STM images of sample A, taken at $V_s = 30$ mV at $T \sim 9$ K (the lower inset) and ~ 82 K ($> T_c$) (the upper inset), and cut along the $(0, 0)$ - $(0, \pi)$ line in the Fourier maps at various bias voltages. The Fourier amplitude is normalized by the intensity of the Bragg peak except the amplitude at the lowest bias, which is normalized so that its background level agrees with those for other biases. (b) Fourier map of the STM image of sample B, taken at $V_s = 30$ mV at $T \sim 9$ K (the inset), and cut along the $(0, 0)$ - $(0, \pi)$ line at various bias voltages. The Fourier amplitude is also normalized by the intensity of the Bragg peak.

In Fig. 4(b), the Fourier map of the STM image and its line cut along the $(\pi, 0)$ direction are shown for sample B. The $q = (1/4, 0)$ Fourier peak appears up to $V_s = 50$ mV, with a very weak peak at $q = (3/4, 0)$. The intensity of the $q = (1/4, 0)$ peak, normalized with the Bragg peak at $q = (1, 0)$, is much weaker than that of sample A. The $q = (1/4, 0)$ peak decreases with V_s and becomes very weak above $V_s \sim 50$ mV. In the line cut of the Fourier

map for sample B as well as sample A, peak structures are observed at $q < 0.2$. However, the intensity of these peaks is almost independent of V_s , meaning that these structures are irrelevant to the 2-d superstructure we focused on (Figs. 4(a) and (b)). The present nondispersive $4a \times 4a$ superstructure observed in samples A and B is essentially the same as the nondispersive $4a \times 4a$ charge order with the internal structure of $4a/3 \times 4a/3$ reported by Hanagri *et al.* for lightly doped Na-CCOC.¹

Shown in Fig. 5(a) is part of a low-bias STM image taken on sample C at $V_s = 30$ mV, which was cut from a single crystal with $T_c \sim 78$ K ($p \sim 0.14$). The 2-d superstructure also appears throughout the entire STM image, as in sample A. Figure 5(b) shows the line profiles of STM images taken along the solid line shown in Fig. 5(a). The superstructure has a period of $\sim 4a$, but its amplitude is weaker than that observed for sample A. The superstructure disappears at a high bias of 80 mV. On the other hand, in the low-bias STM image of sample D, which was cut from the same single crystal as sample C, we can hardly identify a 2-d superstructure (Fig. 5(c)). This means that the $4a \times 4a$ superstructure is very weak in sample D.

Shown in the inset of Fig. 6(a) is the Fourier map $F(q_x, q_y)$ of an STM image taken on sample C at $V_s = 30$ mV. In the present Fourier map, the Fourier transform was carried out excluding top-right corner of the total STM image measured over the area of ~ 38 nm \times 38 nm, where the main Fourier peak is seemingly split into multiple peaks because of local distortion of the superstructure. The line cut of the Fourier map along the $(\pi, 0)$ direction is shown as a function of V_s in Fig. 6(a). The Fourier peaks associated with the 2-d superstructure appear at $q = (0.24, 0)$ and $(0.74, 0)$ and at $q = (0, 0.24)$ and $(0, \sim 0.7)$. The period of the 2-d superstructure of sample C, $4.2a \times 4.2a$ ($\pm 0.2a$), slightly deviates from the commensuration, in contrast to the superstructures of samples A and B. The period $4.2a \times 4.2a$ is referred to as $\sim 4a \times 4a$, including the periodicity of just $4a \times 4a$ observed for samples A and B, hereafter. The $\sim 4a \times 4a$ superstructure of sample C is nondispersive, like those of samples A and B, as seen in Fig. 6(a). It should be noted here that the intensity of the main Fourier peak associated with the $\sim 4a \times 4a$ superstructure of sample C largely depends on bias voltage V_s ; the peak-intensity is very weak at the lowest bias ($V_s = 10$ mV), but rapidly grows with the increase of V_s and reaches the maximum at around $V_s = 20 - 30$ mV, where the Fourier peak becomes much stronger than the Bragg peaks (Fig. 6(a)). The intensity of the Fourier peak largely decreases above $V_s \sim 30$ mV and becomes very weak above $V_s \sim 60$ mV. The $4.2a \times 4.2a$ superstructure of sample C, slightly deviated from the commensuration, reminds us of the weakly dispersive, roughly $4a \times 4a$ structure of the LDOS maps that results from the SC quasiparticle scattering interference.^{6,7} However, the present bias dependence of the wave numbers $q = (0.24, 0)$ and $(0, 0.24)$ is too small to be explained in terms of SC quasiparticle scattering

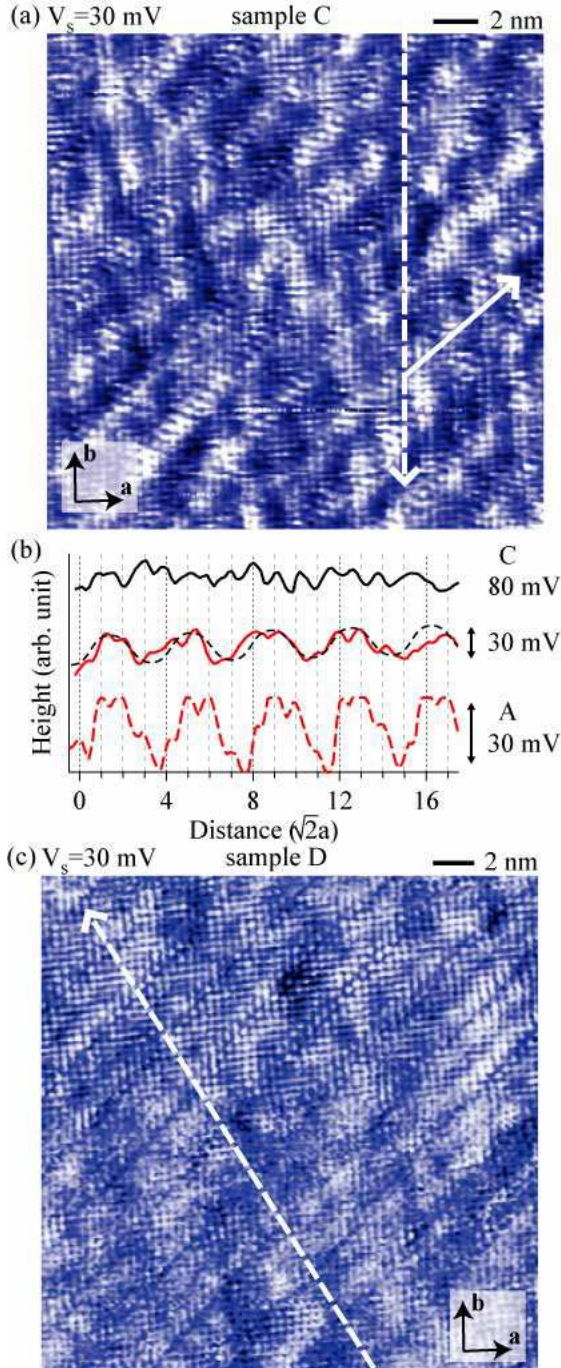


FIG. 5: (Color online) (a) Part of an STM image of sample C, measured at $V_s = 30$ mV and $I_t = 0.3$ nA at $T \sim 9$ K, showing a $4a \times 4a$ superstructure. (b) Line profiles, taken along the solid line in STM image (a), at different bias voltages (the solid lines). For comparison, the line profile at $V_s = 30$ mV for sample A (Fig. 2(b)) is also shown (the dashed line). The dashed line for sample C is a guide to the eye. (c) Part of an STM image of sample D, measured at $V_s = 30$ mV and $I_t = 0.3$ nA at $T \sim 9$ K, showing a very weak $4a \times 4a$ superstructure.

interference.⁷ Furthermore, the $q = (0.24, 0)$ Fourier peak at $V_s = 20 - 30$ mV as intense as the Bragg peak can also hardly be understood from the standpoint of the SC quasiparticle scattering interference. In Fig. 6(b), the Fourier map of the STM image and its line cut along the $(\pi, 0)$ direction are shown for sample D. We can identify the $\sim 4a \times 4a$ superstructure only in the Fourier map for $V_s = 30$ mV, although it is very weak.

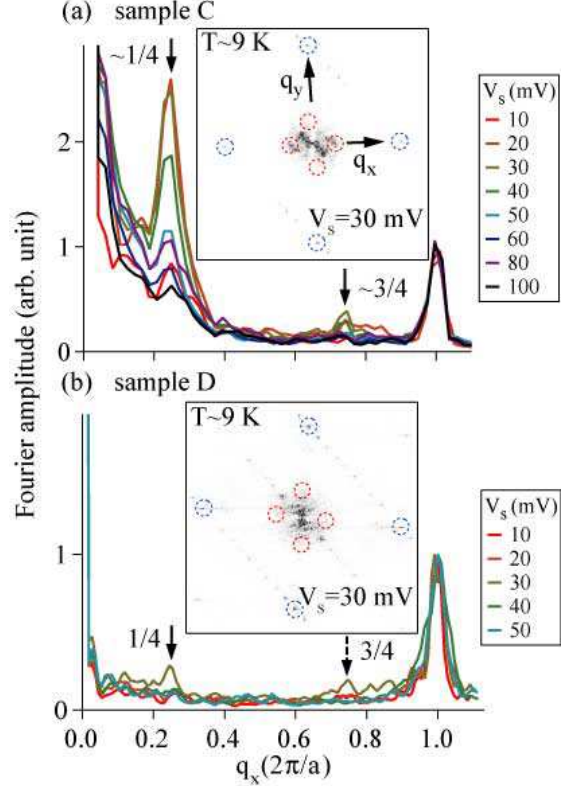


FIG. 6: (Color) Line cuts of 2-d Fourier maps of STM images along the $(0,0)$ - $(0,\pi)$ line at various bias voltages for (a) sample C and (b) sample D. Here the Fourier amplitude is normalized by the intensity of the Bragg peak. The insets of (a) and (b) are Fourier maps of Fig. 5(a) and Fig. 5(c), respectively.

B. Results of STS; superconducting gap structure and $\sim 4a \times 4a$ charge order

Shown in Fig. 7(a) is the spatial dependence of STS spectra for sample A, which exhibits an intense $\sim 4a \times 4a$ charge order throughout its entire low-bias STM image. Many of the STS spectra show the asymmetric V-shaped ZTPG, but some show a symmetric V-shaped gap with no peaks at the gap edge. Thus, the gap structure of sample A is spatially heterogeneous and inhomogeneous as well. In Fig. 7(b), the spatially averaged spectrum over a distance of ~ 40 nm is shown together with the ZTPGs reported for lightly doped Na-CCOC and Bi2212.^{1,2} The

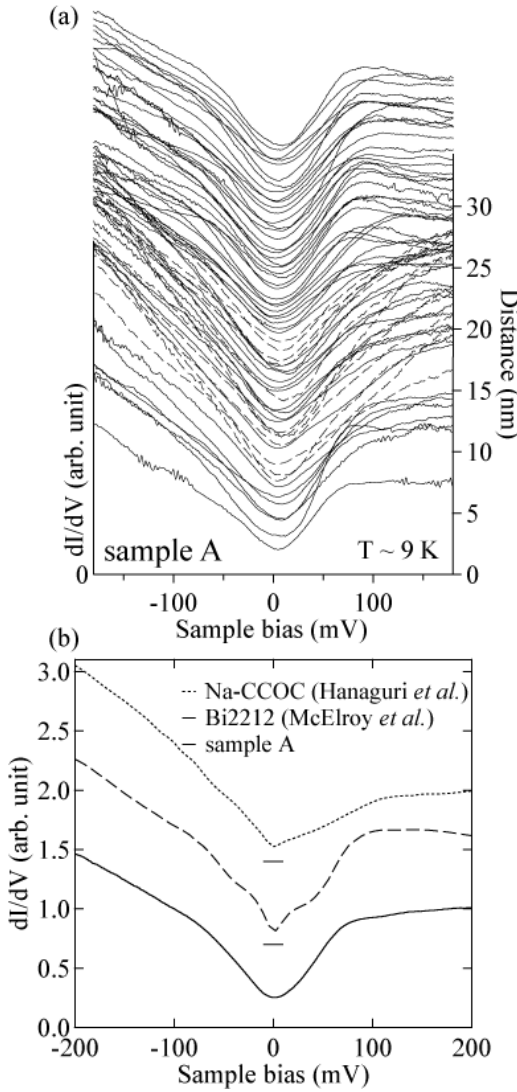


FIG. 7: (a) Spatial dependence of STS spectra at $T \sim 9$ K for sample A. Solid and dashed lines represent the asymmetric V-shaped ZTPG and the symmetric V-shaped gap with no peaks at the gap edge. (b) STS spectrum averaged over a distance of ~ 40 nm on the cleaved surface of sample A at $T \sim 9$ K. Typical ZTPG spectra of lightly doped Na-CCOC (dotted line) and Bi2212 (dashed line) are also shown for comparison.^{1,2}

averaged gap structure is very similar to the ZTPGs of Na-CCOC and Bi2212. Width Δ_0 of the averaged gap, defined as the width between a shoulder on the positive bias side and zero bias $V_s = 0$, is ~ 80 meV. In Fig. 8, the spatial dependence of STS spectra is shown for sample B, whose low-bias STM image exhibits a weak $\sim 4a \times 4a$ superstructure locally. Interestingly the STS spectra of sample B exhibit a homogeneous gap structure of the d -wave type. Gap width Δ_0 , defined as half of the peak-to-peak width, is ~ 56 meV although it tends to be slightly enhanced over the region where the $\sim 4a \times 4a$ superstructure appears clearly.

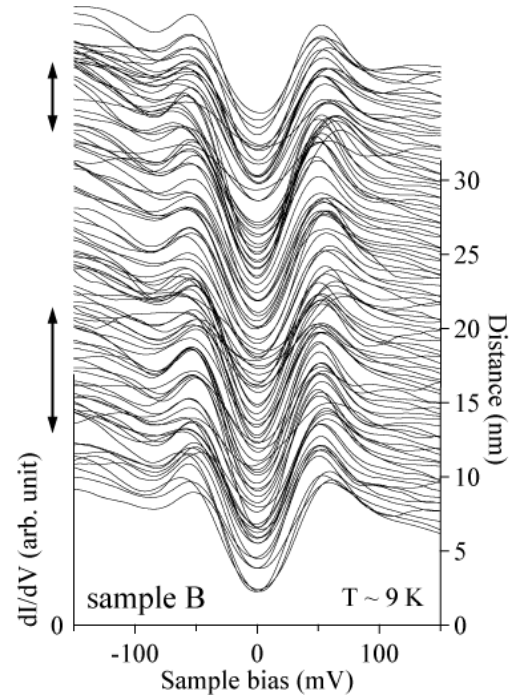


FIG. 8: Spatial dependence of the STS spectra of sample B, taken at $T \sim 9$ K along the dashed line in Fig. 3(b). Two-headed arrows beside the spectra indicate the regions where the $4a \times 4a$ superstructure is clearly observed.

In Fig. 9(a), the STS spectra are shown for sample C, which exhibits an intense $\sim 4a \times 4a$ superstructure throughout its entire low-bias STM image. It should be stressed that the STS spectra are spatially inhomogeneous. Representative gap structures contained in the STS spectra of Fig. 9(a) are shown in Fig. 9(b). The gap structure ranges from a typical d -wave type to an asymmetric V-shaped type with no peaks at the gap edges, and a gap with larger width tends to be accompanied by a subgap. The variation of gap structure shown in Fig. 9(b) is very similar to that reported by McElroy *et al.* for underdoped Bi2212 crystals.² It should be noted that the gap structure around the bottom is almost the same among all the STS spectra of sample C, although the entire gap structure is largely different among them, as seen in Fig. 9(b). This means that the quasiparticle states around the nodes, which dominate the gap structure around the bottom, are homogeneous, and so the inhomogeneity of the gap structure should be attributable to the nature of quasiparticle states away from the nodes, namely, around the antinodes (Fig. 10). In sharp contrast to sample C, the gap structure of sample D, exhibiting a very weak $\sim 4a \times 4a$ superstructure, is spatially homogeneous and of the d -wave type with $\Delta_0 \sim 48$ meV, as shown in Fig. 11(a). In Fig. 11(b), the spatially averaged STS data of samples C and D are shown for comparison. Note that the gap structure around the bottom, $V_s < |20|$ mV, is the same in samples C and D, which were both

cut from the same single crystal. The agreement means that the pairing gap structure around the node is almost the same in sample pair C and D, indicating that the doping level is not so different between the samples.

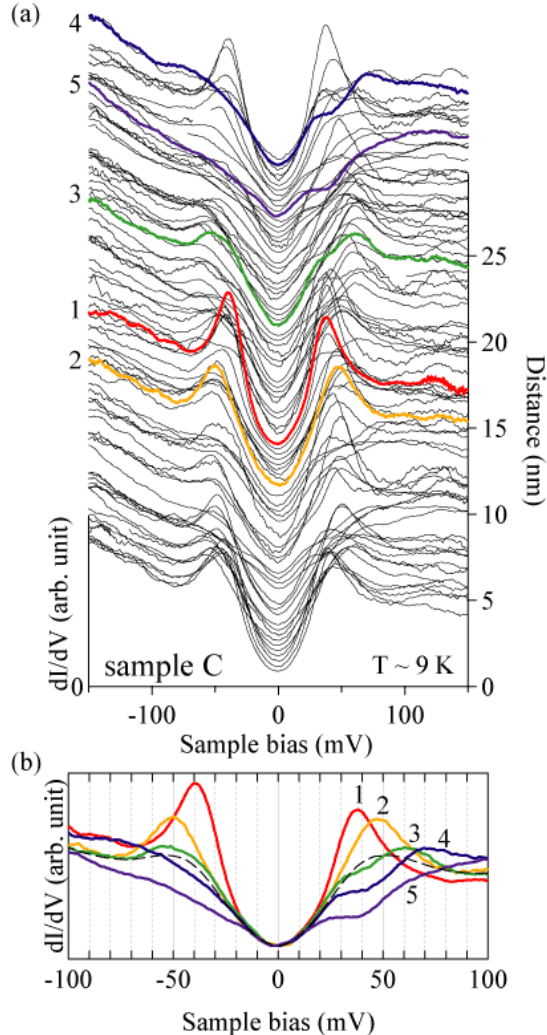


FIG. 9: (Color) Spatial dependence of STS spectra of sample C, taken along the dashed line with a length of ~ 40 nm at $T \sim 9$ K in Fig. 5(a). Typical gap structures are colored. (b) Typical gap structures, represented by the colored lines in Fig. (a), are shown together with the STS spectrum averaged over all the STS spectra of Fig. (a).

It should be emphasized here that both STS spectra of samples A and C, which exhibit intense $\sim 4a \times 4a$ superstructures throughout their entire low-bias STM images, are very inhomogeneous (heterogeneous) spatially, while those of samples B and D exhibiting the weak and/or local superstructure are rather homogeneous. Such interrelation between the inhomogeneous gap structure and the $\sim 4a \times 4a$ superstructure was confirmed on other samples cut from the same single crystal as samples C and D. In the present study, the STS measurements were carried out on the same area of the cleaved surface where

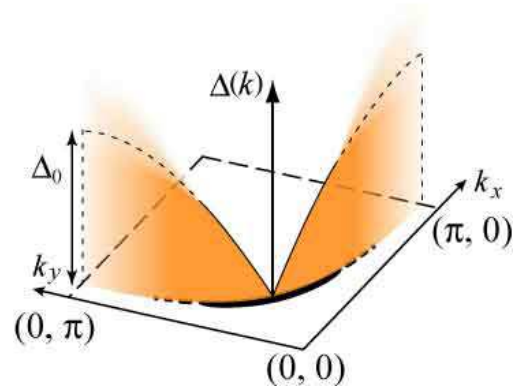


FIG. 10: (Color online) Illustration for “the Fermi arc.” Note that the pairing gap is inhomogeneous around the antinodes near $(\pi, 0)$ and $(0, \pi)$.

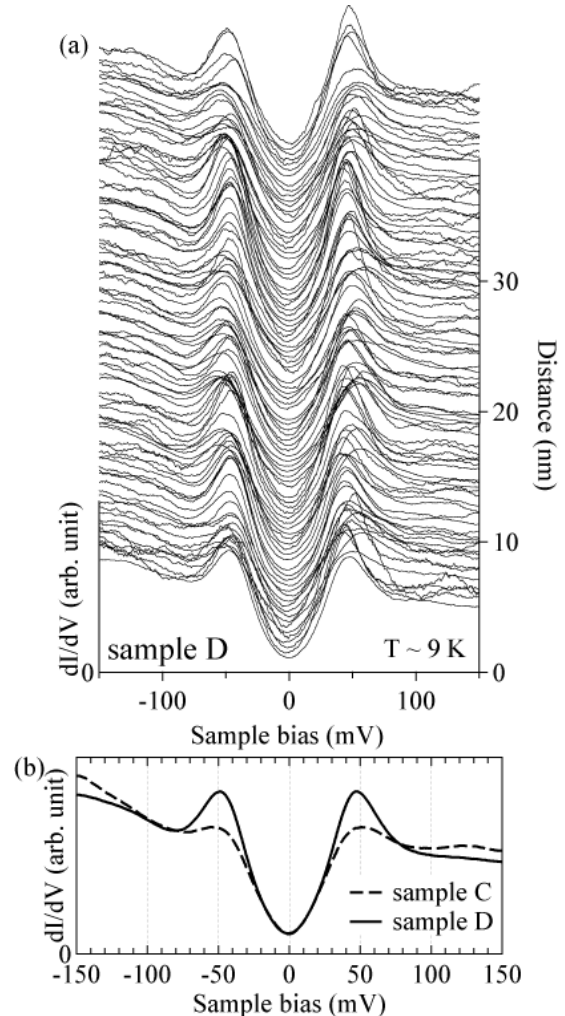


FIG. 11: (a) Spatial dependence of STS spectra of sample D, taken along the dashed line with a length of ~ 40 nm at $T \sim 9$ K in Fig. 5(c). (b) STS spectra averaged over all spectra of samples C and D are shown for comparison.

STM images were taken. Thus, the inhomogeneous gap structure, relating with the nature of quasiparticle states around the antinodes, is intrinsic to the $\sim 4a \times 4a$ superstructure states. This indicates that the quasiparticle states around the antinodes are inhomogeneously modified in the $\sim 4a \times 4a$ superstructure state. McElroy *et al.* have reported that the nondispersive $\sim 4a \times 4a$ superstructure, caused by a charge order, brings about a severe decoherence effect on quasiparticle states around the antinodes, and they claimed that the observation of the charge order is restricted to outside of the pairing gap with $\Delta_0 \gtrsim 65$ meV.² However, this is not the present case, where the $\sim 4a \times 4a$ superstructure appears conspicuously within the gap structure with $\Delta_0 \lesssim 65$ meV, as shown in Fig. 12. In this figure, the intensity of the $\sim 4a \times 4a$ superstructure is shown as a function of bias voltage V_s , together with the gap structure. Interestingly, the $\sim 4a \times 4a$ superstructure appears at $V_s \lesssim \Delta_0/e$, namely, within the pairing gap with Δ_0 . If the $\sim 4a \times 4a$ superstructure is due to some kind of lattice distortion, it is difficult to explain why the superstructure appears within a limited bias (energy) range, especially, associated with gap size Δ_0 ; $V_s \lesssim \Delta_0/e$. Such a limitation for V_s in observing the $\sim 4a \times 4a$ superstructure means that the superstructure is electronic in origin, that is, due to an electronic charge order, as has been claimed in previous studies.^{1–3,8–10} The appearance of the $\sim 4a \times 4a$ charge order within the pairing gap implies that quasiparticles of the SC state and/or hole pairs will take part in causing the charge order.

C. Pinned $\sim 4a \times 4a$ charge order and inhomogeneous gap structure

In high- T_c cuprates, since gap width Δ_0 largely depends on doping level p , the value of Δ_0 measured by STS provides information about doping level p of Cu-O layers near the cleaved surface.^{22,23} Gap width Δ_0 of sample A, exhibiting the intense $\sim 4a \times 4a$ charge order, is larger than that of sample B, exhibiting the weak $\sim 4a \times 4a$ charge order locally. This means that doping level p of sample A is lower than that of sample B, although both samples were cut from the same single crystal. Furthermore, low-bias STM imaging of slightly underdoped Bi2212 with $\Delta_0 \sim 35$ meV exhibits no $\sim 4a \times 4a$ charge order, as was previously reported.²⁰ These results indicate that low doping favors the development of the $\sim 4a \times 4a$ charge order.

Doping level p of sample B is lower than that of sample C, because Δ_0 of sample B is larger than that of sample C. Therefore, a more intense $\sim 4a \times 4a$ charge order could be expected to appear in sample B compared with the charge order of sample C. However, the $\sim 4a \times 4a$ charge order of sample B is weak and only appears locally in the low-bias STM image, whereas sample C exhibits an intense charge order throughout its entire low-bias STM image (Figs. 3(b) and 5(a)). In addition to this result,

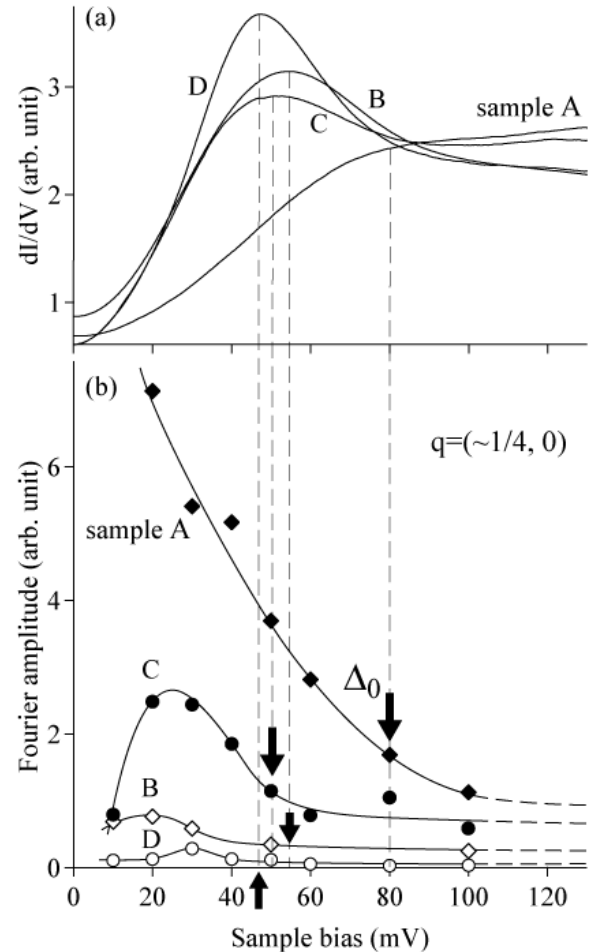


FIG. 12: (a) Averaged STS spectra of samples A, B, C, D on the positive bias side ($V_s \geq 0$). (b) Energy (bias) dependence of the Fourier amplitude at $q \sim 1/4$ for samples A, B, C, D. The arrow shows the sample bias V_s corresponding to gap size Δ_0 in the averaged STS spectrum shown in Fig. (a).

the $\sim 4a \times 4a$ charge order is much weaker in sample D than in sample C, although the doping level is not so different between the samples, as mentioned above. These results indicate that doping level is not the only crucial factor necessary for the development of the nondispersive $\sim 4a \times 4a$ charge order; there is some other important factor in addition to the doping level. It should be emphasized here that sample B shows homogeneous STS spectra with a *d*-wave gap, as mentioned above. The specific, homogeneous *d*-wave gap in sample B means that doping level p is rather homogeneous and hole-pairs are uniformly formed throughout Cu-O layers in this sample. Presumably the $\sim 4a \times 4a$ electronic charge order will develop dynamically throughout Cu-O layers, and it will be pinned down locally over the region with effective pinning centers in sample B. The pinning of the dynamical charge order enables us to observe it in STM measurements. From the standpoint of this pinning picture, the marked difference of the $\sim 4a \times 4a$ charge order

between samples C and D, with similar doping levels, can be explained as the difference in the density and/or strength of pinning centers.

The Bi2212 crystals used in the present study belong to the pseudogap regime. In the pseudogap regime, the Fermi surface can be classified into coherent and incoherent parts; the former is centered at the nodal point of the d -wave gap and often referred to as “the Fermi arc”, whereas the latter is around the antinodes, that is, outside the Fermi arcs (Fig. 10).^{24–31} This heterogeneous structure of the Fermi surface in the pseudogap regime can provide a possible reason why quasiparticle and/or hole-pair states become inhomogeneous on the incoherent parts of the Fermi surface in the intense, pinned $\sim 4a \times 4a$ charge order state. This is because the incoherent electronic states around the antinodes, where the pseudogap develops at $T > T_c$, are easily modified by external perturbations, that is, the randomness associated with the pinning potential in the pinned $\sim 4a \times 4a$ charge order state.

From the standpoint of the present pinning picture, the $\sim 4a \times 4a$ charge order can be expected to appear in STM images when the incoherent quasiparticle states around the antinodes (outside the Fermi arcs) contribute to the STM tunneling. In samples with Fermi arcs of a finite size, like underdoped sample C, no $\sim 4a \times 4a$ charge order will appear in the STM images at very low biases, where only coherent quasiparticles with very low excitation energy on the Fermi arcs contribute to the STM tunneling. However, the $\sim 4a \times 4a$ charge order will appear at higher biases, where incoherent quasiparticles with high excitation energies outside the Fermi arcs contribute to the STM tunneling, as observed experimentally in sample C. On the other hand, in heavily underdoped samples A and B with very tiny Fermi arcs, it is plausible that the $\sim 4a \times 4a$ charge order appears in STM images even at very low biases. This is because there are incoherent quasiparticles with very low excitation energies just outside the tiny Fermi arcs, and they contribute to the STM tunneling even at very low biases.

D. Pinning center and missing atom rows on the Bi-O layer

It is worth while noting that sample A has many more missing atom rows on the cleaved Bi-O layer than sample B, as seen in high-bias STM images reflecting the Bi-O layer (Figs. 2(a) and 3(a)). If the missing atom rows are introduced within the Bi-O layer during the process of cleaving the crystal, some excess oxygen atoms contained within the Bi-O layers will also be removed around the missing atom rows at the same time, which leads to a reduction of the doping level of the Cu-O layer near the cleaved surface. Thus, the high density of the missing atom rows on the cleaved surface of sample A can be a possible reason why the doping level of sample A is lower near the cleaved surface than that of sample B with no

missing atom rows on its cleaved surface, although both samples were cut from the same single crystal. Furthermore, the missing atom rows may play a role as the pinning center for the dynamical $\sim 4a \times 4a$ electronic charge order. In fact, the low density of the missing atom rows on the cleaved surface of sample B can explain the weak, local $\sim 4a \times 4a$ charge order in this sample as well as its homogeneous electronic structure.

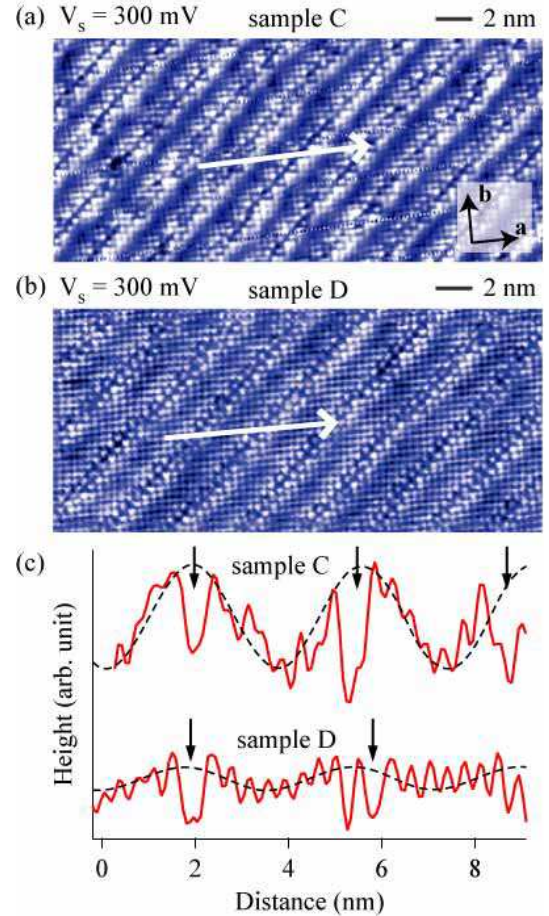


FIG. 13: (Color online) Parts of high-bias STM images of (a) sample C and (b) sample D, measured at $V_s = 300$ mV and $I_t = 0.3$ nA at $T \sim 9$ K. (c) Line profiles for samples C and D, taken along the solid lines shown in (a) and (b), respectively. The line profiles for samples C and D are normalized so that the amplitudes of individual atoms agree with each other in the line profiles for both samples C and D. The dashed lines are guide for the eye and the arrows indicate atomic defects.

On the other hand, we can find no evident difference in the density of missing atom rows on the cleaved surfaces between samples C and D. This is consistent with the fact that the samples have similar doping levels on their cleaved surfaces. Therefore, if the samples C and D have similar pinning centers, these samples are expected to show the $\sim 4a \times 4a$ charge orders with comparable intensities. However, the $\sim 4a \times 4a$ charge order is much stronger in sample C than in sample D, as mentioned

above. This means that sample C will contain other pinning centers different from missing atom rows, although we cannot elucidate what kinds of pinning center they are. The high-bias STM images show that the amplitude of the 1-d superlattice, formed on the Bi-O layer, is evidently larger in sample C than in sample D, as shown in Fig. 13. This large amplitude of the 1-d superlattice may relate to the effective pinning center in sample C. Because the large amplitude of the 1-d superlattice can give rise to inhomogeneous distribution of excess oxygen atoms within Bi-O layers, defects on the Bi-O and Cu-O layers and/or geometrical distortions in the array of atoms around the 1-d superlattice, which could all play roles as pinning centers.³²

IV. SUMMARY

We performed low-bias STM imaging on underdoped SC Bi2212 crystals, and confirmed that the nondispersing $\sim 4a \times 4a$ electronic charge order appears within the pairing gap at $T < T_c$. The present nondispersing charge order is consistent with the findings in the LDOS maps for the SC state of Bi2212 by Howald *et al.* and for the pseudogap state ($T > T_c$) by Vershinin *et al.*^{3,8,9} Howald *et al.* have claimed that the nondispersing charge order results from the formation of the stripe order, though this scenario does not so straightforwardly explain why the observation of the $\sim 4a \times 4a$ charge order is restricted to within the pairing gap.^{8,9,33-35} The appearance of the charge order within the pairing gap is not inconsistent with the models of pair density waves, electronic supersolids, paired-hole Wigner crystallization, or the co-existence of multi-type SC and spin density wave.³⁶⁻⁴⁶

Vershinin *et al.* have claimed that the nondispersing $\sim 4a \times 4a$ charge order at $T > T_c$ is a hidden order of the electron system in the pseudogap state ($T > T_c$).³ In that case, the observation that the nondispersing charge order survives even in the SC state means that the hidden order of the pseudogap state will remain essentially unchanged down to below T_c . It is urgently desired to elucidate how the charge order in the pseudogap state ($T > T_c$) evolves into the nondispersing one in the superconducting state.

We pointed out in the present study that the sample dependence of the nondispersing $\sim 4a \times 4a$ charge order can be understood qualitatively from the standpoint of the pinning picture, which indicates that the $\sim 4a \times 4a$ charge order is dynamical in itself and pinned down over regions with effective pinning centers. The dynamical $\sim 4a \times 4a$ charge order is a possible candidate for the hidden order in the pseudogap regime of pure bulk crystals with no effective pinning centers. We also pointed out that the pairing gap of samples exhibiting the intense, pinned $\sim 4a \times 4a$ charge order is spatially rather inhomogeneous. The inhomogeneous gap structure can be attributable to incoherent electronic (quasiparticle) states around the antinodes, where the pseudogap develops at $T > T_c$. The electronic (quasiparticle) states will be largely modified there by randomness associated with the pinning potential of the $\sim 4a \times 4a$ charge order.

Thanks to useful discussions for Professor F. J. Ohkawa, Professor Z. Tešanović and Professor K. Maki. This work was supported in part by Grant-in-Aid for Scientific Research and the 21st century COE program “Topological Science and Technology” from the Ministry of Education, Culture, Sports, Science and Technology of Japan.

¹ T. Hanaguri, C. Lupien, Y. Kohsaka, D.-H. Lee, M. Azuma, M. Takano, H. Takagi, and J. C. Davis, *Nature* **430**, 1001 (2004).

² K. McElroy, D.-H. Lee, J. E. Hoffman, K. M. Lang, J. Lee, E. W. Hudson, H. Eisaki, S. Uchida, and J. C. Davis, *Phys. Rev. Lett.* **94**, 197005 (2005).

³ M. Vershinin, S. Misra, S. Ono, Y. Abe, Y. Ando, and A. Yazdani, *Science* **303**, 1995 (2004).

⁴ J. E. Hoffman, E. W. Hudson, K. M. Lang, V. Madhavan, H. Eisaki, S. Uchida, and J. C. Davis, *Science* **295**, 466 (2002).

⁵ G. Levy, M. Kugler, A. A. Manuel, Ø. Fischer, and M. Li, *cond-mat/0503219* (unpublished).

⁶ J. E. Hoffman, K. McElroy, D.-H. Lee, K. M. Lang, H. Eisaki, S. Uchida, and J. C. Davis, *Science* **297**, 1148 (2002).

⁷ K. McElroy, R. W. Simmonds, J. E. Hoffman, D.-H. Lee, K. J. Orenstein, H. Eisaki, S. Uchida, and J. C. Davis, *Nature* **422**, 592 (2003).

⁸ C. Howald, H. Eisaki, N. Kaneko, M. Greven, and A. Kapitulnik, *Phys. Rev. B* **67**, 014533 (2003).

⁹ A. Fang, C. Howald, H. Eisaki, N. Kaneko, M. Greven, and A. Kapitulnik, *Phys. Rev. B* **70**, 214514 (2004).

¹⁰ N. Momono, A. Hashimoto, Y. Kobatake, M. Oda, and M. Ido, *J. Phys. Soc. Jpn.* **74**, 2400 (2005).

¹¹ S. H. Pan, J. P. O’Neal, R. L. Badzey, C. Chamon, H. Ding, J. R. Engelbrecht, Z. Wang, H. Eisaki, S. Uchida, A. K. Gupta, et al., *Nature* **413**, 282 (2001).

¹² K. M. Lang, V. Madhavan, J. E. Hoffman, E. W. Hudson, H. Eisaki, S. Uchida, and J. C. Davis, *Nature* **415**, 412 (2002).

¹³ B. W. Hoogenboom, K. Kadowaki, B. Revaz, and Ø. Fischer, *Physica C* **391**, 376 (2003).

¹⁴ A. Matsuda, T. Fujii, and T. Watanabe, *Physica C* **388-389**, 207 (2003).

¹⁵ G. Kinoda, S. Nakao, T. Motohashi, Y. Nakayama, K. Shimizu, J. Shimoyama, K. Kishio, T. Hanaguri, K. Kitazawa, and T. Hasegawa, *Physica C* **388-389**, 273 (2003).

¹⁶ K. Matsuda, H. Sakata, T. Mochiku, K. Hirata, and N. Nishida, *Physica C* **388-389**, 281 (2003).

¹⁷ N. Momono, A. Hashimoto, Y. Kobatake, S. Nakamura, M. Oda, and M. Ido, *Int. J. Mod. Phys. B* **19**, 231 (2005).

¹⁸ M. Oda, H. Matsuki, and M. Ido, *Solid State Commun.* **74**, 1321 (1990).

¹⁹ T. Nakano, M. Oda, C. Manabe, N. Momono, Y. Miura, and M. Ido, Phys. Rev. B **49**, 16000 (1994).

²⁰ M. Oda, C. Manabe, and M. Ido, Phys. Rev. B **53**, 2253 (1996).

²¹ C. Renner and Ø. Fischer, Phys. Rev. B **51**, 9208 (1995).

²² M. Oda, K. Hoya, R. Kubota, C. Manabe, N. Momono, T. Nakano, and M. Ido, Physica C **281**, 135 (1997).

²³ N. Miyakawa, P. Guptasarma, J. F. Zasadzinski, D. G. Hinks, and K. E. Gray, Phys. Rev. Lett. **80**, 157 (1998).

²⁴ M. R. Norman, H. Ding, M. Randeria, J. C. Campuzano, T. Yokoya, T. Takeuchi, T. Takahashi, T. Mochiku, K. Kadowaki, P. Guptasarma, et al., Nature **392**, 157 (1998).

²⁵ T. Yoshida, X. J. Zhou, T. Sasagawa, W. L. Yang, P. V. Bogdanov, A. Lanzara, Z. Hussain, T. Mizokawa, A. Fujimori, H. Eisaki, et al., Phys. Rev. Lett. **91**, 27001 (2003).

²⁶ F. Ronning, T. Sasagawa, Y. Kohsaka, K. M. Shen, A. Damascelli, C. Kim, T. Yoshida, N. P. Armitage, D. H. Lu, D. L. Feng, et al., Phys. Rev. B **67**, 165101 (2003).

²⁷ Y. Yanase and K. Yamada, J. Phys. Soc. Jpn. **68**, 548 (1999).

²⁸ D. Pines, Physica C **282-287**, 273 (1997).

²⁹ V. B. Geshkenbein, L. B. Ioffe, and A. I. Larkin, Phys. Rev. B **55**, 3173 (1997).

³⁰ N. Furukawa, T. M. Rice, and M. Salmhofer, Phys. Rev. Lett. **81**, 3195 (1998).

³¹ X.-G. Wen and P. A. Lee, Phys. Rev. Lett. **80**, 2193 (1998).

³² K. McElroy, J. Lee, J. A. Slezak, D.-H. Lee, H. Eisaki, S. Uchida, and J. C. Davis, Science **309**, 1048 (2005).

³³ S. A. Kivelson, E. Fradkin, , and V. J. Emery, Nature **393**, 550 (2001).

³⁴ M. Bosch, W. van Saarloos, and J. Zaanen, Phys. Rev. B **63**, 092501 (2001).

³⁵ S. A. Kivelson, I. P. Bindloss, E. Fradkin, V. Oganesyan, J. M. Tranquada, A. Kapitulnik, and C. Howald, Rev. Mod. Phys. **75**, 1201 (2003).

³⁶ M. Vojta, Phys. Rev. B **66**, 104505 (2002).

³⁷ M. Ichioka and K. Machida, J. Phys. Soc. Jpn. **71**, 1836 (2002).

³⁸ D. Podolsky, E. Demler, K. Damle, and B. I. Halperin, Phys. Rev. B **67**, 094514 (2003).

³⁹ H.-D. Chen, O. Vafek, A. Yazdani, and S.-C. Zhang, Phys. Rev. Lett. **93**, 187002 (2004).

⁴⁰ S. Sachdev and E. Demler, Phys. Rev. B **69**, 144504 (2004).

⁴¹ Z. Tešanović, Phys. Rev. Lett. **93**, 217004 (2004).

⁴² M. Franz, Science **305**, 1410 (2004).

⁴³ P. W. Anderson, cond-mat/0406038 (unpublished).

⁴⁴ H. C. Fu, J. C. Davis, and D.-H. Lee, cond-mat/0403001 (unpublished).

⁴⁵ H. Won, S. Haas, D. Parker, and K. Maki, Phys. Stat. Sol. B **242**, 363 (2005).

⁴⁶ F. J. Ohkawa, cond-mat/0510829 (unpublished).